Mechanisms of the Antibacterial Effects of TiO$_2$–FeO$_x$ under Solar or Visible Light: Schottky Barriers versus Surface Plasmon Resonance

John Kiwi * and Sami Rtimi

Ecole Polytechnique Fédérale de Lausanne, EPFL-SB-GPAO Station 6, CH-1015 Lausanne, Switzerland; sami.rtimi@epfl.ch

* Correspondence: john.kiwi@epfl.ch; Tel.: +41-21-693-6150

Abstract: This study reports the significant mechanistic difference between binary-oxide antibacterial films with the same composition but different microstructures. Binary TiO$_2$-FeO$_x$ films were found to present a faster bacterial inactivation kinetics under visible light irradiation than each single oxide acting independently. The interaction between the film active surface species and the bacteria within the disinfection period was followed by X-ray photoelectron spectroscopy (XPS) and provided the evidence for a redox catalysis taking place during the bacterial inactivation time. The optical and surface properties of the films were evaluated by appropriate surface analytical methods. A differential mechanism is suggested for each specific microstructure inducing bacterial inactivation. The surface FeO$_x$ plasmon resonance transferred electrons into the conduction band of TiO$_2$ because of the Schottky barrier after Fermi level equilibration of the two components. An electric field at the interface between TiO$_2$ and FeO$_x$, favors the separation of the photo-generated charges leading to a faster bacterial inactivation by TiO$_2$–FeO$_x$ compared to the bacterial inactivation kinetics by each of the single oxides.

Keywords: antibacterial films; sputtering; visible light; surface microstructure; mechanism; ROS identification

1. Introduction

Photocatalytic nanomaterials such as TiO$_2$ are receiving a great deal of attention owing to their potential applications in environmental remediation [1,2]. Nonetheless, the low efficiency of this class of materials under solar irradiation, absorbing <5% of the incident light, limits their performance in photo-induced processes. At the present time, there is a need to develop more efficient TiO$_2$ composite photocatalysts, active under visible light [3–5]. Hybrid nanostructured composite photocatalysts like binary oxides seem a fruitful solution. The present mini-review addresses hybrid, stable, adhesive antibacterial TiO$_2$–FeO$_x$ films leading to visible light-driven bacterial inactivation. We describe briefly the properties of TiO$_2$ and Fe oxides (FeO$_x$) and address the preparation, evaluation, and properties of TiO$_2$–FeO$_x$ films having the same composition but different microstructures.

TiO$_2$ is known to exhibit photocatalytic antimicrobial activity over a broad spectrum of microorganisms. The antimicrobial properties of TiO$_2$ are attributed to the high redox potential of reactive oxygen species (ROS) generated on TiO$_2$ under band-gap irradiation. Foster et al. [6], Yadav et al. [7], Kiwi et al. [8], Kubacka et al. [9], Verdier et al. [10], Al-Hazmi et al. [11], and others have recently reported a comprehensive review of the photocatalytic disinfection properties of TiO$_2$. The first report on bacterial sterilization by TiO$_2$ powders was published by Matsunaga et al. [12]. TiO$_2$ under band-gap irradiation photo-induces charge carriers that subsequently in the presence of O$_2$ lead to ROS with high oxidative potentials. These ROS are effective in pollutant abatement, bacterial

inactivation, or both. When the oxidant used exceeds the natural antioxidant defenses in a bacterial strain, death cell follows through a complex set of redox reactions. Natural antioxidants like carotene, ascorbic acid, tocopherol inhibit lipid peroxidation or O-singlet effects [13] and the effects of ROS radicals such as $HO_2^{\bullet-}$ and $^{\bullet}OH$ which are effective in biological inactivation.
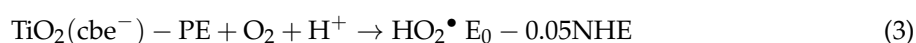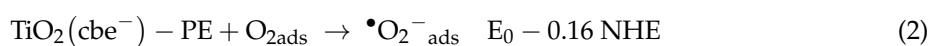
Iron oxide thin film have extensive applications in semiconductor devices, magneto-optic memories, audio-video systems, computer chips, and memory storage devices. Iron oxide exists in three phases: α-Fe_2O_3, β-Fe_2O_3, γ-Fe_2O_3 [14]. α-Fe_2O_3 with a band gap of 2.2 eV absorbs in the visible up to 570 nm and its charges present a low hole diffusion length and short exciton lifetime (~10 ps). Iron oxide shows antibacterial behavior [15]. ROS generated by α-Fe_2O_3 induce physical damage by contact leading to bacterial reduction [16–18]. The genotoxicity of Fe oxides is currently investigated in medical research against cancer. The oxidative damage introduced by Fe, FeO_x, Fe_2O_3, and Fe_3O_4 nanoparticles (NPs) reduces or destroys cancer cells but concomitantly induces cellular injury or death in normal cells. Fe oxides lead to genetically regulated cell death (apoptosis) and to an increase of the ROS levels by damage within cells, followed by autophagy. The potential damage to tissues located behind cellular barriers needs to be considered when using Fe NPs for targeting tumors [19–21]. Super-paramagnetic iron oxide particles combined with certain chemicals are labelled SPIONS and increase ROS stress up to a factor of 10 during cancer cell treatment. Coupling SPIONS with X-ray radiotherapy amplifies the cytotoxicity on tumors and cancer cells. This is a synergistic strategy [22]. Because of the complexity of this field, this mini-review addresses only the interaction of binary oxides containing FeO_x NPs with simpler probes like bacteria and the details related to the bacterial damage and destruction.
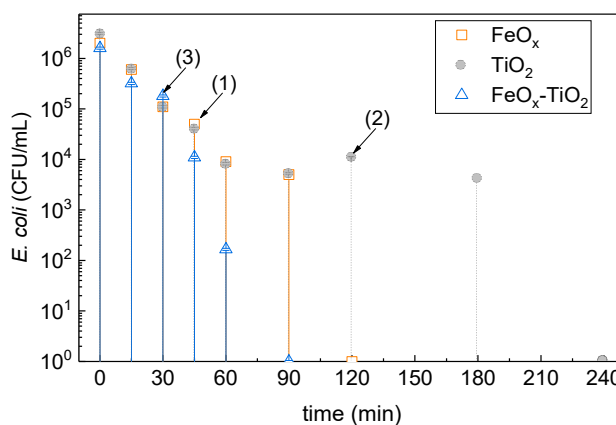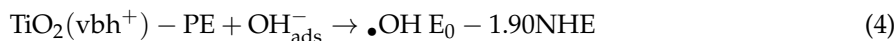
Fe(III)-modified titania and Fe(III)–Ti(IV) binary oxides have received little attention as photocatalyst films compared to their parent single metal oxides, Fe_2O_3 and TiO_2. This is due to the difficulty of obtaining a pure mono-phase TiO_2. In addition, the effect of different preparative conditions on films prepared by sol–gel as well as their surface properties, catalytic and photocatalytic activity have been the object of very few studies [23–27]. In colloidal formulations up to 10%, FeO_x can be added and will disperse well in the TiO_2 lattice. The addition of higher percentages of FeO_x leads to Fe-phase segregation. Very little work has been reported on the detailed microstructure of TiO_2–FeO_x stable, uniform, adhesive films. This moved us to investigate the films microstructure effect on the bacterial inactivation kinetics. Surface properties and reaction mechanism leading to bacterial killing is reported by the binary-oxide composites.

2. TiO_2–FeO_x Surfaces Leading to Bacterial Inactivation under Solar Light with a Faster Kinetics Compared to Either TiO_2 or FeO_x Films

Dispersions of $FeCl_3$ and TiO_2 Degussa P25 were prepared using $FeCl_3$ (100 mg L^{-1}) and TiO_2 (5 g L^{-1}) and were irradiated to photo-corrode polyethylene (PE) and introduce negatively charged oxidative sites able to bind both oxides by exchange–adsorption and electrostatic interaction. The photo-corrosion of the TiO_2 powder surfaces was carried out under UV irradiation for 15 h. After UV irradiation, the films were sonicated in aqueous solution for 10 min to remove loosely bound oxide particles, washed, and dried for 10 min at 80 °C. This operation was repeated two times, and the films were dried at 60 °C. Stable TiO_2–FeO_x films were obtained by this procedure.
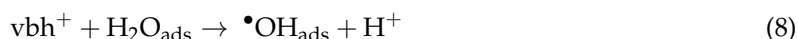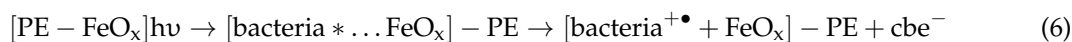
Figure 1 shows the kinetics of bacterial inactivation under low-intensity solar irradiation for TiO_2, FeO_x, and TiO_2–FeO_x. It is readily seen that the binary composite induced a faster bacterial inactivation kinetics compared to each of the single oxides evaluated separately [28]. The main reactions leading to bacterial inactivation on TiO_2 are suggested below in Equations (1)–(5) [2,29]:

$$\text{bacteria} + [TiO_2 - PE]\text{light} \rightarrow [TiO_2^* - PE]\text{bacteria} \rightarrow [\text{bacteria}^* \ldots TiO_2 - PE]\text{cbe}^- \tag{1}$$

$$TiO_2(\text{cbe}^-) - PE + O_{2ads} \rightarrow {}^{\bullet}O_2{}^-{}_{ads} \quad E_0 - 0.16\,\text{NHE} \tag{2}$$

$$TiO_2(\text{cbe}^-) - PE + O_2 + H^+ \rightarrow HO_2{}^{\bullet} \quad E_0 - 0.05\text{NHE} \tag{3}$$

$$\mathrm{TiO_2(vbh^+) - PE + OH^-_{ads} \rightarrow {_\bullet}OH \ E_0 - 1.90NHE} \tag{4}$$

$$\mathrm{TiO_2(vbh^+) - PE + H_2O_{ads} \rightarrow {_\bullet}OH_{ads} + E^+} \tag{5}$$
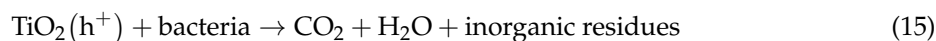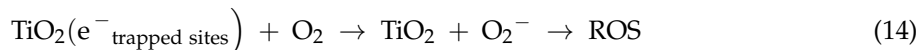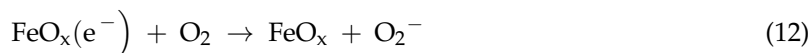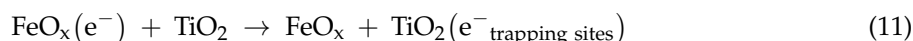

Figure 1. *Escherichia coli* inactivation (CFU/mL) on polyethylene (PE) films coated with (1) FeO_x, (2) TiO_2, and (3) FeO_x–TiO_2 as a function of time of irradiation under low-intensity solar simulated light (50 mW cm^{-2}).

Bacterial inactivation by FeO_x under solar simulated light irradiation could be obtained as noted in Equations (6)–(9):

$$\mathrm{[PE - FeO_x]h\upsilon \rightarrow [bacteria * \ldots FeO_x] - PE \rightarrow [bacteria^{+\bullet} + FeO_x] - PE + cbe^-} \tag{6}$$

$$\mathrm{FeO_x + hv \rightarrow FeO_x(vbh^+)} \tag{7}$$

$$\mathrm{vbh^+ + H_2O_{ads} \rightarrow {}^\bullet OH_{ads} + H^+} \tag{8}$$

$$\mathrm{cbe^- + H_2O_{ads} \rightarrow OH^- + H^+} \tag{9}$$

The acceleration of bacterial inactivation in Figure 1 by the TiO_2–FeO_x photocatalyst can be rationalized in terms of the intervention of FeO_x, injecting e$^-$ into TiO_2, as noted below:

$$\mathrm{FeO_x + light \rightarrow FeO_x(e^-) + FeO_x(h^+)} \tag{10}$$

$$\mathrm{FeO_x(e^-) + TiO_2 \rightarrow FeO_x + TiO_2(e^-_{trapping\ sites})} \tag{11}$$

$$\mathrm{FeO_x(e^-) + O_2 \rightarrow FeO_x + O_2^-} \tag{12}$$

$$\mathrm{{}^\bullet O_2^- + H^+ \rightarrow HO_2^\bullet \rightarrow ROS} \tag{13}$$

$$\mathrm{TiO_2(e^-_{trapped\ sites}) + O_2 \rightarrow TiO_2 + O_2^- \rightarrow ROS} \tag{14}$$

$$\mathrm{TiO_2(h^+) + bacteria \rightarrow CO_2 + H_2O + inorganic\ residues} \tag{15}$$

The mechanism of the reaction between TiO_2–FeO_x–PE and the bacteria under visible light proceeded noted in Equation (1). Under visible light, FeO_x (mainly Fe_2O_3), as it will be described in the paragraph below, would transfer the photo-generated electrons in the conduction band (cbe$^-$) to the lower-lying TiO_2 sites, since FeO_x presents a conduction band (cb) positioned at potential energy values 0.4–0.6 eV, below the anatase trapping states [30]. Leytner et al. [31] identified the electron-trapping sites in anatase positioned at ~0.8 eV below the anatase (cb) by time-resolved photo-acoustic spectroscopy (TRPAS). Gray et al. [32] used electron paramagnetic resonance (EPR) spectroscopy and reported anatase trapping sites located ~0.5–0.8 eV below the anatase (cb). The mechanism for the interfacial charge transfer (IFCT) between Fe_2O_3 and TiO_2 on sol–gel films is suggested in Figure 2.
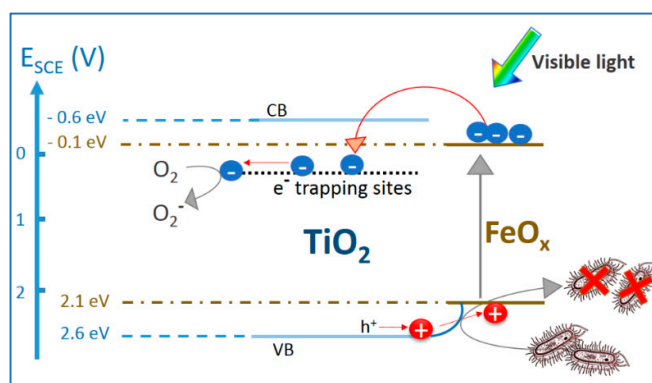
Figure 2. Interfacial charge transfer (IFCT) electron transfer between FeO_x and low-lying TiO_2 trapped states under visible light irradiation (>404 nm). Reprinted with permission from [28]. Copyright 2017 Elsevier.

It is interesting, at this point, to look into the oxidation states of the FeO_x species before and after bacterial inactivation. Figure 3 presents the changes in the Fe oxidation states of PE–FeO_x within the 120 min bacterial inactivation reported in Figure 1, trace (1). Figure 3 shows that the initial $Fe(III)/Fe_2O_3$ at 712.2 eV decreased from ~80.0% at time zero to ~53.0% after bacterial inactivation. Concomitantly, an increase in the Fe_3O_4 at 713.6 eV and $Fe(II)$ at 709.7 eV was observed. The X-ray photoelectron spectroscopy (XPS) shifts were referenced by the values found in reference [33]. Therefore, during the bacterial inactivation period, *redox* reactions occurred on the catalyst surface during bacterial inactivation. After bacterial inactivation, the XPS peak positions for Fe(III), FeO(II/III), and Fe(II) peaks were: 711.4, 708.6, and 713.8 eV, respectively [34]. The three Fe-oxides in Figure 3 intervened with a different potential during bacterial reduction as shown in Figure 3. The surface concentration of the elements were observed to remain fairly stable within the period of bacterial inactivation (see Table 1).
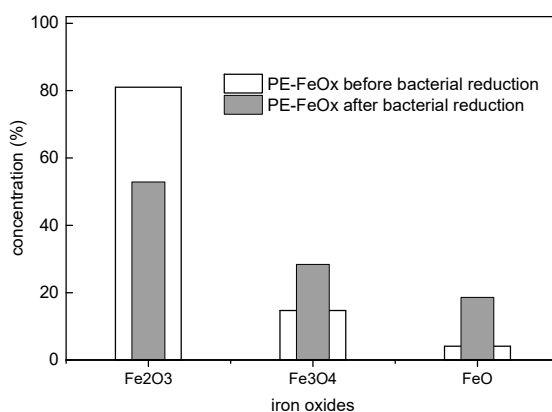

Figure 3. X-ray photoelectron spectroscopy (XPS) of PE–FeO_x films sputtered for 60 s before and after bacterial inactivation under solar simulated light (52 mW cm^{-2}). Reprinted with permission from [35]. Copyright 2015 RSC.

Table 1. Surface atomic percentages concentration determined by XPS on PE–FeO_x sputtered for 60 s before and after bacterial reduction under solar irradiation (52 mW cm^{-2}).

Element	Before	After
Fe2p	7.87	7.39
O1s	31.11	35.27
C1s	61.02	57.34
N2p	0.9	1.19

3. Sputtering of TiO$_2$–Fe$_2$O$_3$ Microstructure to Accelerate the Bacterial Inactivation Kinetics: Process Optimization

Films prepared by sol–gel are not perfectly reproducible, are not robust, are weakly adhesive, and lack uniformity. This is a serious hindrance for antibacterial applications over long periods, for which film stability is a primary consideration. Work by Kelly et al. [35,36] addressed the preparation of stable antibacterial films by sputtering metals and oxides. Sputtering active metals and oxides leads to highly oxidative species, leading to bacterial death. A magnetron sputtering unit is shown in Figure 4. The amounts of the point defects in the aggregates/crystallites films on the substrate are considerably higher than in similar films prepared by sol–gel because of the higher energies during the sputtering process [37]. Defects in oxide crystals and nuclei are located at energies within the band gaps, giving raise to intermediate mid-gap energy states mediating the photo-excited electron transition from the cb band to the valence band (vb) band [38]. Alternatively, they can act as recombination centers depending on their concentration. The rapid inclusion during sputtering, of Fe and O atoms during the sputtering time into the TiO$_2$ film lattice creates O vacancies and interstitial defects. [39]. The higher activity of the sputtered films is in part attributed to an increase in the defects in the crystallites. Oxides like TiO$_2$ and FeO$_x$ have been extensively reported in the literature presenting four type defects: (a) O vacancies, (b) Ti or Fe vacancies, (c) O interstitials, and (d) Ti or Fe interstitials [40,41]. The work in the field of bacterial inactivation films need a more advanced catalysts design and preparation leading to a faster kinetics and a higher absorption in the visible range. Also, a higher reusability threshold is needed for antibacterial films for large scale applications. Section 4 below illustrates how the microstructure of TiO$_2$–FeO$_x$ profoundly affects the bacterial inactivation kinetics.
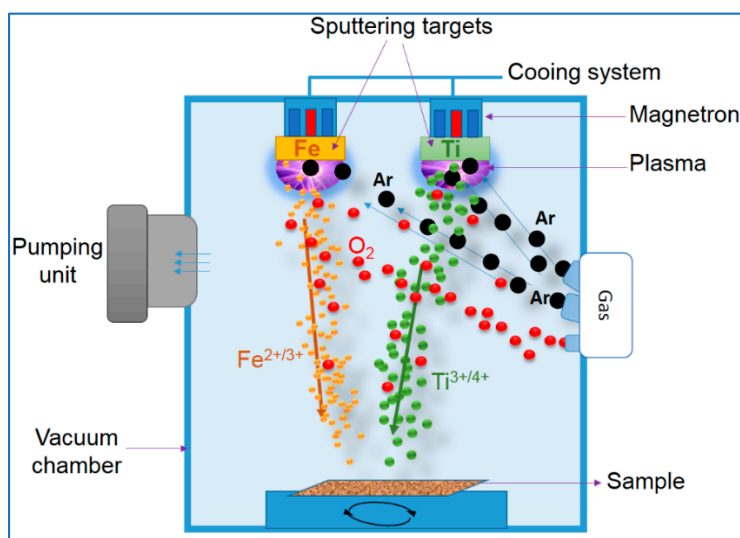

Figure 4. Schematic representation of the two target-sputtering units used to deposit the metal and oxides films in Ar atmosphere with a low residual concentration of air (O$_2$).

4. Optical and Surface Properties of Co-Sputtered and Sequentially Sputtered TiO$_2$–FeO$_x$ Films Active in Bacterial Inactivation

Figure 5 shows the diffuse reflection spectroscopy (DRS) spectra in Kubelka–Munk units for TiO$_2$–PE, FeO$_x$–PE, (a) sequentially sputtered TiO$_2$/FeO$_x$–PE films, and (b) co-sputtered TiO$_2$–FeO$_x$–PE films. The sputtering times noted in the caption of Figure 5 were optimized to find the most suitable ratio TiO$_2$/FeO$_x$ for a film leading to bacterial inactivation kinetics. The TiO$_2$–FeO$_x$ composite absorbs in the visible region >400 nm, inducing TiO$_2$–FeO$_x$ charge transfer bands [42]. The light absorption in the spectral region between 400 and 500 nm in Figure 5 is attributed to IFCT between TiO$_2$ and FeO$_x$. The weak absorption >500 nm is due to the short-lived Fe d–d inter-band transitions. The electron

pair-deficient oxygen vacancy was suggested to be able to react with Ti^{4+}-ions to form Ti^{3+} centers, by Serpone et al. [43]. The amount of vacancies was reported to be one-half of the Fe(III) found in the TiO_2 (Ti^{4+}) network [44–49].
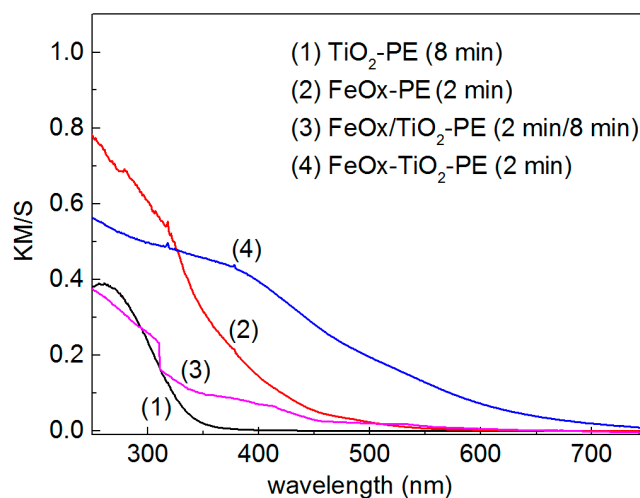

Figure 5. Diffuse reflection spectroscopy (DRS) showing the Fe(III) shifting band gap excitation of TiO_2 to the visible region in the samples: (1) TiO_2–PE (8 min), (2) FeO_x–PE (2 min), (3) sequentially sputtered TiO_2/FeO_x–PE (2 min FeO_x, 8 min TiO_2), and (4) co-sputtered TiO_2—FeO_x–PE (2 min). Reprinted with permission from [39]. Copyright 2015 RSC.

The roughness (R_g) of the co-sputtered TiO_2–FeO_x–PE films was ~24 nm, as determined by atomic force microscopy (AFM). A value of ~11 nm was found for the sequentially sputtered TiO_2/FeO_x–PE films. The co-sputtered films showed FeO_x nano-particle sizes of 15–30 nm and TiO_2 nano-particle sizes of 10–15 nm. The particle size, diffusion, and mass transport determine particle growth and surface roughness [50]. The sequential sputtered films showed FeO_x NPs sizes of 20–40 nm. The bigger size of the sequentially sputtered NPs compared to the co-sputtered films is attributed to an easier collective diffusion in the FeO_x top-most layers of the latter samples [51]. The deposition of the co-sputtered TiO_2–FeO_x–PE films and the sequentially sputtered TiO_2/FeO_x–PE films was carried in a similar way. Bacterial inactivation mediated by the co-sputtered TiO_2–FeO_x–PE sample was completed within 60 min compared with the 120 min required by the sequentially sputtered samples. Both samples were sputtered for 2 min. Both samples were close in specific surface area (SSA) and that the difference in the bacterial inactivation times could not be ascribed to a difference in the surface area between the samples. The photo-sensitizing role of FeO_x unexpectedly led to similar inactivation times under solar simulated light and under visible light in both samples (404 nm cut-off filter).

5. Evidence by XPS of Bacterial Inactivation Inducing Differentiated Redox Interactions with TiO_2–FeO_x Samples

Figure 6a presents the changes in the Fe oxidation states for sequentially sputtered TiO_2/FeO_x–PE films. The initial Fe_2O_3 was seen to increase from ~70% at time zero to ~80% after 30 min at the expense of Fe_3O_4 and FeO. The Fe oxide peaks were referenced by the values reported in reference [33]. Figure 6b shows the changes of FeO_x and TiO_2 oxidation states in the co-sputtered films within the disinfection time. The initial 60% Fe_2O_3 percentage remained constant during the disinfection time, and the Fe_3O_4 and FeO percentages were conserved up to 60 min, while TiO_2 (Ti^{4+}) slightly increased with a concomitant decrease of Ti^{3+}-oxidation state. Electrostatic attraction occurs between the negatively charged *Escherichia coli* at pH 6–7 and the slightly positive TiO_2–FeO_x–PE surface. The interaction between reactants at distances below 4–8 Å is accompanied by a strong polarization at these short distances [52,53]. Fe_2O_3 presents a cb at +0.1 eV and a vb at +2.2 eV [1,2]. The valence band holes (vbh^+) interact with the adsorbed –OH surface groups but do not have a potential high

enough to lead to the formation of $^\bullet$OH radicals, since the transformation $^\bullet$OH–OH$^-$ requires 1.90 eV. The HO$_2$$^\bullet$ radicals oxidize bacteria undergoing concomitantly HO$_2$$^\bullet$–HO$_2$$^-$ reduction at 0.75 eV. This is a significant lower potential compared to that required by the transformation $^\bullet$OH–OH$^-$. The HO$_2$$^\bullet$ decomposes at pH > 4.8, driving the pH to acidic values, as shown below in Equation (16):

$$HO_2^\bullet + Fe^{3+} \rightarrow Fe^{2+} + O_2 + H^+ \tag{16}$$
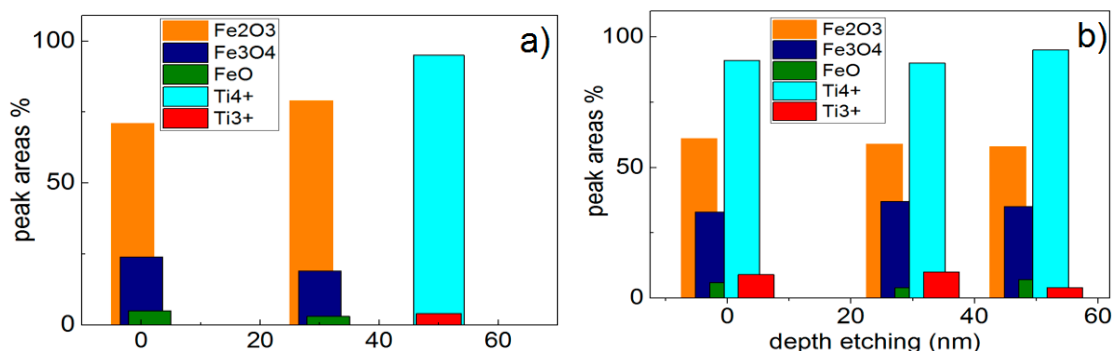
Figure 6. (**a**) Evolution of Ti2p and Fe2p oxidation states during bacterial inactivation as a function of the disinfection time, as determined by XPS for: (**a**) sequentially sputtered TiO$_2$/FeO$_x$–PE films, (**b**) co-sputtered TiO$_2$–FeO$_x$–PE films. Irradiation source: Suntest simulated (52 mW cm^{-2}) in the presence of a cut-off filter at 400 nm. Reprinted from [54].
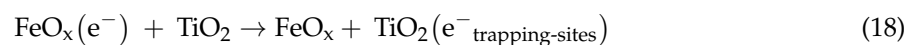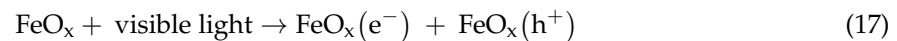
Figure 7a presents the XPS for the sequentially sputtered films. Figure 7a shows the atomic percentage composition as a function of the etching depth for Fe, Ti, and O. The etching of the film surface was carried out by sputtering Ar ions of 5 kV. These Ar ions are able to reach a depth of ~50 nm (~250 layers). The TiO$_2$ under-layers in Figure 7 were only detected up to 30 nm and reached an atomic concentration of 60% after sputtering Ar ions for 45 nm. The O-enrichment level was stable at 25%–30% up to 65 nm. Figure 7b shows that the surface atomic percentage of the Ti and Fe layers was similar within 50 nm (250 atomic layers). The amount of O in the surface was close to those of TiO$_2$ and FeO$_x$ at ~30%. Figure 7a,b show the drastic differences in the microstructure of the TiO$_2$–FeO$_x$ films for the sequential and co-sputtered samples.
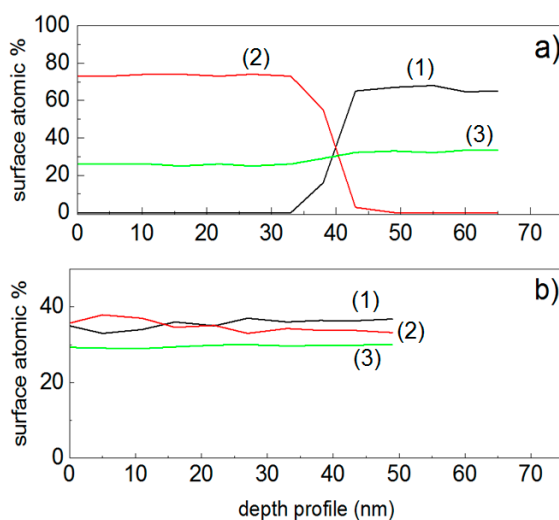

Figure 7. XPS etching by way of a beam of 5 kV Ar ion for: (**a**) sequentially sputtered TiO$_2$/FeO$_x$-PE films, (1) Ti2p, (2) Fe2p, and (3) O1s; (**b**) Co-sputtered TiO$_2$–FeO$_x$–PE films showing the atomic percentage concentration of atoms, (1) Ti2p, (2) Fe2p, and (3) O1s in the topmost layers (2 nm) as a function of the penetration depth. Reprinted from [54].

## 6. The Role of the Microstructure Controlling the Bacterial Inactivation Mechanism: Critical Issues

The schematic intervention of co-sputtered FeO_x–TiO_2 leading to bacterial inactivation is suggested in Figure 8a. The mixed TiO_2–FeO_x–PE film led to charge separation and involved quasi-Fermi equilibration between the two oxides. The FeO_x electron transfer to low-lying TiO_2 trapping states is shown in Figure 8a. The co-sputtered TiO_2–FeO_x–PE films induced a faster bacterial inactivation compared to the sequentially sputtered TiO_2/FeO_x–PE. A decrease in the film FeO_x electron-hole recombination rate occurred in the co-sputtered TiO_2-FeO_x films. Some steps involving the transfer of Fe_2O_3 cb (e^-) into the TiO_2 trapping sites are noted below:

$$FeO_x + \text{visible light} \rightarrow FeO_x(e^-) + FeO_x(h^+) \tag{17}$$

$$FeO_x(e^-) + TiO_2 \rightarrow FeO_x + TiO_2(e^-_{\text{trapping-sites}}) \tag{18}$$

$$TiO_2(h^+) + \text{bacteria} \rightarrow \text{inorganic/organic residues} \tag{19}$$

In the sequentially sputtered TiO_2/FeO_x–PE film as shown in Figure 8b, the FeO_x topmost layers absorbed the visible light reaching the sample surface [36,39,54]. The incorporation of Fe oxides into the crystal lattice of wide band-gap semiconductors (such as TiO_2) improved the photocatalytic activity of TiO_2 in the visible-light region because of the surface plasmon resonance (SPR) effect of FeO_x [55,56]. The surface plasmon resonance arises from the collective oscillations of electrons on the surfaces of metals and oxides, and these surface transfer electrons into the conduction band of TiO_2 because of the Schottky barrier. The Schottky barrier between FeO_x and TiO_2 arises as a consequence of the Fermi level equilibration between TiO_2 and FeO_x. This favors the separation of the photo-generated charges, as noted in Figure 9 [57,58].
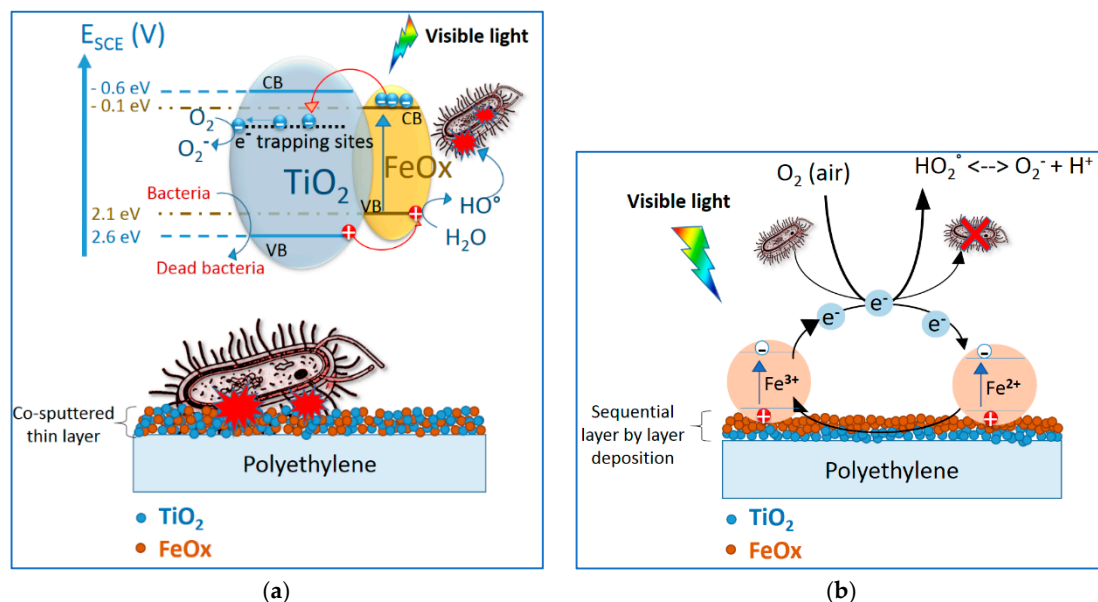

Figure 8. (**a**) IFCT leading to bacterial inactivation under visible light induced by co-sputtered by TiO_2–FeO_x–PE films. For further details, see the text. (**b**) Simplified mechanism for bacterial inactivation by sequentially sputtered TiO_2/FeO_x–PE films under visible light. For further details, see the text.
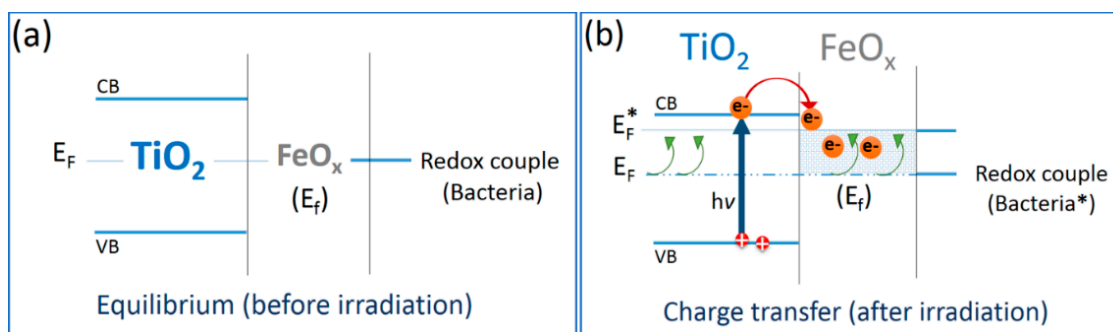
Figure 9. Equilibration of TiO_2–FeO_x nanocomposites with redox couple (bacteria) (**a**) before and (**b**) after irradiation.

Figure 10a shows that the TiO_2 nanocomposites irradiated with solar energy photons, having energy higher than the TiO_2 band gap, photo-excited electrons from the valance band to the conduction band, leaving holes in the valance band. Figure 10b shows the IFCT at the TiO_2-FeO_x heterojunction under visible light. The close contact between FeO_x NPs and TiO_2 in the sputtered films acts as an electron sink to promote the reduction of oxygen on their surfaces. Subsequently, the holes in the valence band of TiO_2 migrated, inducing bacterial oxidation. A local electric field developed by the SPR of FeO_x in contact with TiO_2. The increased charge separation, due to the FeO_x NPs sputtered on TiO_2, increased the lifetime of the TiO_2 charge-carriers. This was due to FeO_x partly substituting the lattice Ti^{4+} sites in TiO_2, which modifies the visible light absorbance of TiO_2. Takeuchi [59] has recently reported metal implantation on TiO_2 films, increasing the film photocatalytic activity. Figure 8b consisting only of FeO_x NPs (in the TiO_2/FeO_x–PE film) is a film made up by a single component. In this case, a faster charge recombination of the photo-induced charges occurs, limiting the amount of charges available for the photocatalytic reactions leading to bacterial inactivation [60].
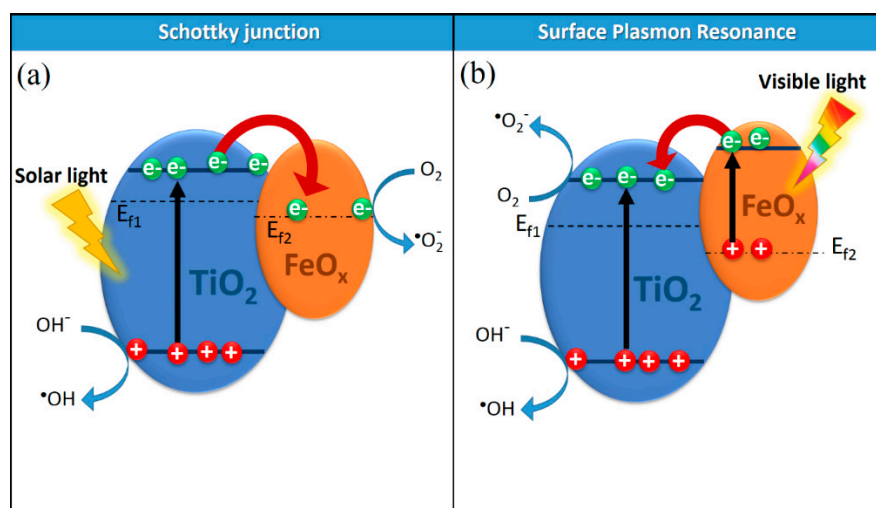
Figure 10. IFCT at the TiO_2–FeO_x heterojunction under (**a**) solar light irradiation (UV-component) and (**b**) under visible-light irradiation.

7. Conclusions

This work describes the modification strategies of TiO_2 to prepare more performing binary oxides employable in photocatalysis. Basic concepts related to the surface modification of TiO_2 by FeO_x are discussed. Further, this review suggests basic mechanisms for photo-chemical processes as a function of the film microstructure. The heterojunction between FeO_x and TiO_2 promotes a directional electron flow in the co-sputtered films, leading to a faster bacterial inactivation. FeO_x and TiO_2 deposition in the films follow a random distribution. The photochemical intervention in bacterial inactivation processes

were a function of the sputtering time and applied sputtering energy. The redox reactions taking place during bacterial inactivation were monitored by XPS within the disinfection time. The co-sputtered FeO_x–TiO_2–PE films were shown to lead to a faster bacterial inactivation kinetic. These films show the potential to prevent biofilm formation under sun or visible light. This mini-review may be useful to orient the work on low-cost, stable TiO_2-films for pollutants degradation and bacterial inactivation with enhanced absorption in the visible region.

Author Contributions: S.R. carried out the sputtering, biological evaluation, and surface characterization of the films. J.K. oriented the content of the work and the layout of the final write-up. Both authors approved the submitted manuscript and are accountable for the material presented.

Conflicts of Interest: The authors declare no conflict of interest.

Abbreviations

cb	conduction band
vb	valence band
cbe^-	photo-generated electrons in the conduction band
vbh^+	photo-generated holes in the valence band
FeO_x	iron oxides
TiO_2	titanium dioxide
PE	polyethylene
TiO_2/FeO_x–PE	sequentially sputtered TiO_2 followed by FeO_x deposition
TiO_2–FeO_x–PE	co-deposition of TiO_2 and FeO_x (at the same time)
EPR	electron paramagnetic resonance
IFCT	interfacial charge transfer
ROS	reactive oxygen species
XPS	X-ray Photo-electron Spectroscopy
R_g	roughness
DRS	diffuse reflectance spectroscopy
SSA	specific surface area
TRPAS	time-resolved photo-acoustic spectroscopy

References

1. Byrne, J.A.; Dunlop, P.S.M.; Hamilton, J.W.J.; Fernandez-Ibanes, P.; Polo-Lopez, I.; Sharma, K.P.; Vennard, M.S.A. A review of heterogeneous photocatalysis for water and surface disinfection. *Molecules* **2015**, *20*, 5574–5615. [CrossRef] [PubMed]

2. Rtimi, S.; Sanjines, R.; Pulgarin, C.; Kulik, A.; Kiwi, J. Innovative transparent non-scattering TiO_2 bactericide films inducing increased *E. coli* cell fluidity. *Surf. Coat. Technol.* **2014**, *254*, 333–343. [CrossRef]

3. Pelaez, M.; Nolan, N.T.; Pillai, S.C.; Seery, M.K.; Falaras, P.; Kontos, A.G.; Dunlop, P.S.M.; Hamilton, J.W.J.; Byrne, A.J.; O'Shea, K.; et al. A review on the visible light active titanium dioxide photocatalysts for environmental applications. *Appl. Catal. B* **2012**, *125*, 331–349. [CrossRef]

4. Banerjee, S.; Pillai, C.S.; Falaras, P.; O'Shea, K.; Byrne, A.-J.; Dionysiou, D. New insights into the mechanism of visible light photocatalysis. *J. Phys. Chem. Lett.* **2014**, *5*, 2543–2554. [CrossRef] [PubMed]

5. Banerjee, S.; Dionysiou, D.; Pillai, C.S. Self-cleaning applications of TiO_2 by photo-induced hydrophilicity and photocatalysis. *Appl. Catal. B* **2015**, *176–177*, 396–428. [CrossRef]

6. Foster, H.; Ditta, I.; Varghese, S.; Steele, A. Photocatalytic disinfection using titanium dioxide: Spectrum and mechanism of antimicrobial activity. *Appl. Microbiol. Biotechnol.* **2011**, *90*, 1847–1868. [CrossRef] [PubMed]

7. Yadav, H.; Kiwi, J.; Pawar, S.H. Development in photocatalytic antibacterial activity of nano TiO_2: A review. *Korean J. Chem.* **2016**, *33*, 1989–1998. [CrossRef]

8. Rtimi, S.; Pulgarin, C.; Kiwi, J. Recent developments in accelerated antibacterial inactivation on 2D Cu-titania surfaces under indoor visible light. *Coatings* **2017**, *7*, 20. [CrossRef]

9. Kubacka, A.; Diez, M.; Rojo, D.; Ciordia, S.; Zapico, I.; Albar, J.; Barbas, C.; Martins dos Santos, V.; Fernandez-Garrcia, M.; Ferrer, M. Understanding the Antimicrobial mechanism of TiO_2 based nano-composite films in a pathogenic bacterium. *Sci. Rep.* **2014**, *4*, 4134–4143. [CrossRef] [PubMed]

10. Verdier, T.; Coutand, M.; Bertron, A. Antibacterial activity of TiO_2 photocatalyst alone or in coatings on *E. coli*: The influence of methodological aspects. *Coatings* **2014**, *4*, 670–686. [CrossRef]

11. Alhadrami, H.A.; Al-Hazmi, F. Antibacterial activities of titanium oxide nanoparticles. *J. Bioelectron. Nanotechnol.* **2017**, *2*, 5.

12. Matsunaga, T.; Tomoda, R.; Nakajima, T.; Wake, H. Photoelectrochemcal sterilization of microbial cells by semiconductor powders. *FEMS Microbiol. Lett.* **1985**, *29*, 211–214. [CrossRef]

13. Jones, D.P. Redefining oxidative stress. *Antioxid. Redox Signal.* **2006**, *8*, 1865–1879. [CrossRef] [PubMed]

14. Yogi, A.; Varshney, D. Magnetic and structural properties of pure and Cr-doped hematite: α-$Fe_{2-x}Cr_xO_3$ ($0 \leq x \leq 1$). *J. Adv. Ceram.* **2013**, *2*, 360–369. [CrossRef]

15. Basnet, P.; Larsen, G.K.; Jadeja, R.P.; Hung, Y.C.; Zhao, Y. α-Fe_2O_3 nano-columns and nano-rods fabricated by electron beam evaporation for visible light photocatalytic and antimicrobial applications. *ACS Appl. Mater. Inter.* **2013**, *5*, 2085–2095. [CrossRef] [PubMed]

16. Zhang, W.; Rittmann, B.; Chen, Y. Size effects on adsorption of hematite nanoparticles on *E. coli* cells. *Environ. Sci. Technol.* **2011**, *45*, 2172–2178. [CrossRef] [PubMed]

17. Ubale, A.U.; Belkhedkar, M.R. Size dependent physical properties of nanostructured α-Fe_2O_3 thin films grown by successive ionic-layer deposition and reaction method for antibacterial application. *J. Mater. Sci. Technol.* **2015**, *31*, 1–9.

18. Jana, T.K.; Pal, A.; Mandal, A.K.; Sarwar, S.; Chakrabarti, P.; Chatterjee, K. Photocatalytic and antibacterial performance of α-Fe_2O_3 nanostructures. *ChemistrySELECT* **2017**, *2*, 3068–3077.

19. Golbamaki, N.; Rasuley, B.; Cassano, A.; Robinson, N.; Benfebati, E.; Leszczynski, J.; Cronin, T. Genotoxicity of metal oxide nanomaterials: Review of recent data and discussion of possible mechanisms. *Nanoscale* **2015**, *14*, 2154–2198. [CrossRef] [PubMed]

20. Bhabra, B. Nanoparticles can cause DNA damage across a cellular barrier. *Nat. Nanotechnol.* **2009**, *4*, 876–883. [CrossRef] [PubMed]

21. Schulz, E.; Wenzel, P.H.; Munzel, T.H.; Daiber, A. Mitochondrial redox signaling: Interaction of mitochondrial reactive oxygen species with other sources of oxidative stress. *Antioxid. Redox Signal.* **2014**, *20*, 308–324. [CrossRef] [PubMed]

22. Klein, S.; Sommer, A.; Distel, V.; Hazeman, L.; Kroner, W.; Neuhuber, W.; Muller, P.; Proux, O.; Kryshxhi, C. Superparamagnetic iron oxide nanoparticles as novel X-ray enhancer for low-dose radiation therapy. *J. Phys. Chem. B* **2014**, *118*, 6159–6166. [CrossRef] [PubMed]

23. Wachs, I. Recent conceptual advances in the catalysis science of mixed metal oxide catalytic materials. *Catal. Today* **2005**, *100*, 79–94. [CrossRef]

24. Pal, B.; Maheshwar, S.; Gyoichi, N. Preparation and characterization of TiO_2/Fe_2O_3 binary mixed oxides and its photocatalytic properties. *Mater. Chem. Phys.* **1999**, *59*, 254–261. [CrossRef]

25. Rong, L.; Jia, Y.; Bu, N.; Wu, J.; Zhen, Q. Photocatalytic degradation of methyl blue using Fe_2O_3/TiO_2 composite ceramics. *J. Alloy. Compd.* **2015**, *643*, 88–93.

26. Tung, W.; Daoud, W. New approach toward nanozised ferrous ferric oxide and Fe_3O_4-doped titanium dioxide photocatalysts. *Appl. Mat. Interfaces* **2009**, *11*, 2453–2461. [CrossRef] [PubMed]

27. Lazar, M.; Daoud, W. Achieving selectivity in TiO_2-based photocatalysis. *RSC Adv.* **2013**, *3*, 4130–4135. [CrossRef]

28. Camarasa-Mena, A.; Rtimi, S.; Pulgarin, C.; Lavanchy, C.-J.; Kiwi, J. Grafted semiconductors on PE-films leading to bacterial inactivation: Synthesis characterization and mechanism. *Colloids Surf. A* **2017**, *519*, 231–237. [CrossRef]

29. Wardman, P. Reduction potentials of one electron couples involving free radicals in aqueous solutions. *J. Phys. Chem. Ref. Data* **1989**, *18*, 1637–1755. [CrossRef]

30. Fujishima, A.; Zhang, X.; Tryk, D. TiO_2 photocatalysis and related surface phenomena. *Surf. Sci. Reps.* **2008**, *63*, 515–546. [CrossRef]

31. Leytner, S.; Hupp, T. Evaluation of the energetics of electron trap states at the nano-crystalline titanium dioxide/aqueous solution interface via time-resolved photo-acoustic spectroscopy. *Chem. Phys. Lett.* **2000**, *330*, 231–236. [CrossRef]

32. Hurum, C.; Agrios, A.; Gray, K.; Rajh, T.; Thurnauer, M. Explaining the enhanced photocatalytic activity of Degussa P25 mixed-phase TiO_2 using EPR. *J. Phys. Chem. B* **2003**, *107*, 4545–4549. [CrossRef]

33. Wagner, D.; Riggs, M.; Davis, E.; Mullenberg, G. *Handbook of X-ray Photoelectron Spectroscopy*; PerkinElmer: Eden Prairie, MN, USA, 1979.

34. Kelly, P.; Li, H.; Benson, P.; Whitehead, K.; Verran, J.; Arnell, R.; Iordanova, I. Comparison of the tribological and antimicrobial properties of CrN/Ag, ZrN/Ag TiN/Ag and Tin/Cu nanocomposite coatings. *Surf. Coat. Technol.* **2010**, *205*, 1606–1610. [CrossRef]

35. Rtimi, S.; Pulgarin, C.; Sanjines, R.; Kiwi, J. Novel FeO_x polyethylene transparent films: Synthesis and mechanism of surface regeneration. *RSC Adv.* **2015**, *5*, 80203–80211. [CrossRef]

36. Fisher, L.; Ostovapour, S.; Kelly, P.; Whitehead, K.; Cooke, K.; Storgards, E.; Verran, J. Molybdenum doped titanium oxide photocatalytic coating; for use as hygienic surfaces: The effect of soiling on antimicrobial activity. *Biofouling* **2014**, *30*, 911–919. [CrossRef] [PubMed]

37. Mathews, W.J. Nucleation of Thin Films. In *Epitaxial Growth*, 1st ed.; Venables, J., Price, G., Eds.; Elsevier: New York, NY, USA, 1975; pp. 382–435.

38. Koster, G.; Huijben, M.; Rijnders, G. *Epitaxial Growth of Complex Metal Oxides*; Elsevier: Burlington, VT, USA, 2015.

39. Rtimi, S.; Sanjines, R.; Kiwi, J.; Pulgarin, C.; Bensimon, M.; Khmehl, I.; Nadtochenko, V. Innovative photocatalyst (FeO_x-TiO_2): Transients induced by femtosecond laser pulse leading to bacterial inactivation under visible light. *RSC Adv.* **2015**, *5*, 101751–101759. [CrossRef]

40. Bak, T.; Nowotny, J.; Nowotny, M. Defect Disorder of Titanium Dioxide. *J. Phys. Chem. B* **2006**, *110*, 21560–21567. [CrossRef] [PubMed]

41. Kremenović, A.; Antić, B.; Blanuša, J.; Čomor, M.; Colomban, P.H.; Mazerolles, L.; Bozin, E. Heterogeneity and disorder in $Ti_{1-x}Fe_yO_{2-d}$ nanocrystal rutile-based flower like aggregates: Detection of anatase. *J. Phys. Chem. C* **2011**, *115*, 4395–4403. [CrossRef]

42. Yu, H.; Irie, H.; Shimodaira, Y.; Hisogi, Y.; Kuroda, Y.; Miyauchi, M.; Hashimoto, K. An efficient visible-light-sensitive Fe(III)-grafted TiO_2 photocatalyst. *J. Phys. Chem. C* **2010**, *114*, 16481–16486. [CrossRef]

43. Kusnetsov, N.V.; Serpone, N. Visible light absorption by various titanium dioxide specimens. *J. Phys. Chem. B* **2006**, *110*, 25203–25209. [CrossRef] [PubMed]

44. Etacheri, V.; Di Valentin, C.; Schneider, J.; Bahnemann, D.; Pillai, C.S. Visible-light activation of TiO_2 photocatalysts: Advances in theory and experiments. *J. Photochem. Photobiol. C Rev.* **2015**, *25*, 1–29. [CrossRef]

45. Novabpour, P.; Ostorvapour, S.; Tattershall, C.; Cooke, K.; Kelly, P.; Verran, J.; Whitehead, K.; Hill, C.; Raulio, M.; Priha, O. Photocatalytic TiO_2 and doped TiO_2 coatings to improve the hygiene of surfaces in food and beverage processing—A study of the physical and chemical resistance of the coatings. *Coatings* **2014**, *4*, 433–449. [CrossRef]

46. Truppi, A.; Petronella, F.; Placido, T.; Striccoli, M.; Agostiano, A.; Curri, M.L.; Comparelli, R. Visible light active TiO_2 based hybrid nanocatalyst for environmental applications. *Catalysts* **2017**, *7*, 100. [CrossRef]

47. Shakeri, A.; Yip, D.; Badv, M.; Imani, S.; Sanjari, M.; Didar, T. Self-cleaning ceramic tiles produced via stable coatings of TiO_2 nanoparticles. *Materials* **2018**, *11*, 1003. [CrossRef] [PubMed]

48. Wen, K.; Liu, M.; Liu, X.; Deng, C.; Zhou, K. Deposition of photocatalytic coating by modifying the solidification pathway in plasma spraying. *Coatings* **2017**, *7*, 169. [CrossRef]

49. Pasin, L.; Meyer, J.; Eiche, E.; Kasper, G. On the activity enhancing role of iron oxide for noble metal oxidation catalysts: A CVD-based study with differently structured combinations of Pt and FeO_x coatings on Al_2O_3. *Coatings* **2018**, *8*, 217. [CrossRef]

50. Ehiasarian, A. High-power impulse magnetron sputtering and its applications. *Pure Appl. Chem.* **2010**, *82*, 1247–1258. [CrossRef]

51. Wheeler, D.A.; Wang, G.; Ling, Y.; Li, Y.; Zhang, J.Z. Nanostructured hematite: Synthesis, characterization, charge carrier dynamics, and photoelectrochemical properties. *Energy Environ. Sci.* **2012**, *5*, 6682–6702. [CrossRef]

52. Docampo, P.; Guldin, S.; Steiner, U.; Snaith, H.J. charge transport limitations in self-assembled TiO$_2$ photo-anodes for dye-sensitized solar cells. *J. Phys. Chem. Lett.* **2013**, *4*, 698–703. [CrossRef] [PubMed]

53. Adams, D.; Brus, L.; Chidsey, C.; Creager, S.; Creutz, C.; Kagan, C.H.; KamatV, P.; Lieberman, M.; Lindsay, S.; Marcus, M.; et al. Charge transfer on the nanoscale: Current status. *J. Phys. Chem. B* **2003**, *107*, 6668–6697. [CrossRef]

54. Rtimi, S.; Pulgarin, C.; Nadtochenko, V.A.; Gostev, F.E.; Shelaev, I.V.; Kiwi, J. FeO$_x$-TiO$_2$ film with different microstructures leading to femtosecond transients with different properties: Biological implications under visible light. *Sci. Reps.* **2016**, *6*, 30113–30123. [CrossRef] [PubMed]

55. Hung, W.-H.; Chien, T.-M.; Tseng, C.-M. Enhanced photocatalytic water splitting by plasmonic TiO$_2$–Fe$_2$O$_3$ cocatalyst under visible light irradiation. *J. Phys. Chem. C* **2014**, *118*, 12676–12681. [CrossRef]

56. Ghuman, K. Mechanistic insights into water absorption and dissociation on amorphous TiO$_2$-based catalysts. *Sci. Technol. Adv. Mater.* **2018**, *19*, 44–52. [CrossRef] [PubMed]

57. Jing, L.; Zhou, W.; Tian, G.; Fu, H. Surface tuning for oxide-based nanomaterials as efficient photocatalysts. *Chem. Soc. Rev.* **2013**, *42*, 9509–9549. [CrossRef] [PubMed]

58. Rtimi, S.; Kiwi, J. Bactericide effects of transparent polyethylene photocatalytic films coated by oxides under visible light. *Appl. Catal. B* **2017**, *213*, 62–73. [CrossRef]

59. Takeuchi, M.; Yamashita, H.; Matsuoka, M.; Anpo, M.; Hirao, T.; Itoh, N.; Iwamoto, N. Photocatalytic decomposition of NO under visible light irradiation on the Cr-ion-implanted TiO$_2$ thin film photocatalyst. *Catal. Lett.* **2000**, *67*, 135–137. [CrossRef]

60. Rtimi, S. Indoor light enhanced photocatalytic ultra-thin films on flexible non-heat resistant substrates reducing bacterial infection risks. *Catalysts* **2017**, *7*, 57. [CrossRef]